Eur. Phys. J. C (2021) 81:106
https://doi.org/10.1140/epjc/s10052-021-08918-y

THE EUROPEAN PHYSICAL JOURNAL C

Regular Article - Experimental Physics

Search for double β-decay modes of ^{64}Zn using purified zinc

F. Bellini[1,2], M. Beretta[3,4,12], L. Cardani[2], P. Carniti[3,4], N. Casali[2], E. Celi[5,6,a], D. Chiesa[3,4], M. Clemenza[3,4], I. Dafinei[2], S. Di Domizio[7,8], F. Ferroni[2,5], L. Gironi[3,4], Yu. V. Gorbenko[9], C. Gotti[3,4], G. P. Kovtun[9,10], M. Laubenstein[6], S. Nagorny[6,5,13,b], S. Nisi[6], L. Pagnanini[5,6,c], L. Pattavina[6], G. Pessina[4], S. Pirro[6], E. Previtali[3,4], C. Rusconi[6,11], K. Schäffner[5,6], A. P. Shcherban[9], D. A. Solopikhin[9], V. D. Virich[9], C. Tomei[2], M. Vignati[2]

[1] Dipartimento di Fisica, Sapienza Università di Roma, 00185 Rome, Italy
[2] INFN-Sezione di Roma, 00185 Rome, Italy
[3] Dipartimento di Fisica, Università di Milano-Bicocca, 20126 Milan, Italy
[4] INFN-Sezione di Milano-Bicocca, 20126 Milan, Italy
[5] Gran Sasso Science Institute, 67100 L'Aquila, Italy
[6] INFN-Laboratori Nazionali del Gran Sasso, Assergi, 67100 L'Aquila, Italy
[7] Dipartimento di Fisica, Università di Genova, 16146 Genoa, Italy
[8] INFN-Sezione di Genova, 16146 Genoa, Italy
[9] National Science Center Kharkov Institute of Physics and Technology, Kharkov 61108, Ukraine
[10] Karazin Kharkov National University, Kharkov 61022, Ukraine
[11] Department of Physics and Astronomy, University of South Carolina, Columbia, SC 29208, USA
[12] Present Address: University of California, Berkeley, CA 94720, USA
[13] Present Address: Physics Department, Queen's University, Kingston, ON K7L 3N6, Canada

Received: 9 December 2020 / Accepted: 25 January 2021 / Published online: 2 February 2021

Abstract The production of ultra-pure raw material is a crucial step to ensure the required background level in rare event searches. In this work, we establish an innovative technique developed to produce high-purity (99.999%) granular zinc. We demonstrate the effectiveness of the refining procedure by measuring the internal contaminations of the purified zinc with a high-purity germanium detector at the Laboratori Nazionali del Gran Sasso. The total activity of cosmogenic activated nuclides is measured at the level of a few mBq/kg, as well as limits on naturally occurring radionuclides are set to less than mBq/kg. The excellent radiopurity of the zinc sample allows us to search for electron capture with positron emission and neutrinoless double electron capture of ^{64}Zn, setting the currently most stringent lower limits on their half-lives, $T_{1/2}^{\varepsilon\beta^+} > 2.7 \times 10^{21}$ year (90% CI), and $T_{1/2}^{0\nu 2\varepsilon} > 2.6 \times 10^{21}$ year (90% CI), respectively.

1 Introduction

The search for rare events such as dark matter interactions [1] or neutrinoless double-beta decay [2] has an important role in the investigation of physical processes not predicted by the standard model. The common experimental effort for next-generation experiments focuses on the reduction of detector contamination, to reach an extremely low background index. In this scenario, the purification of the initial materials used for the detector construction acquires a pivotal relevance.

Zinc-containing crystals are widely used in rare event physics as room-temperature scintillators ($ZnWO_4$ [3–5]), low-temperature calorimeters (ZnSe in CUPID-0 [6], $ZnMoO_4$ in LUMINEU [7]) or semiconductor detectors (CdZnTe in COBRA [8]).

To understand the importance of the purity of the initial materials, we consider the specific case of ZnSe [9]. The most common production method for these crystals is the growth by melt crystallization under high inert gas pressure, known as Bridgman–Stockbarger technique [10]. With this method large volume crystals can be grown, reaching up to 60 mm in diameter and 2 kg in mass. The downside of this technique is the lack of perfection in the produced crystalline structure. During crystallization, a fraction of the ZnSe compound in the liquid phase dissociates, transferring part of the single components (Zn and Se) to the cold zone. The transfer is due either to diffusion through the semi-penetrable graphite crucible walls, or to evaporation from the free surface of the melt. Because of differences in diffusion coefficients, the melt results enriched in one of the components, causing devi-

[a] e-mail: emanuela.celi@gssi.it
[b] e-mail: sn65@queensu.ca
[c] e-mail: lorenzo.pagnanini@gssi.it (corresponding author)

ations from the stoichiometry that can be significantly larger than 1%. Such a process leads to the formation of intrinsic point defects (IPD) in the crystalline structure, affecting both the scintillating and bolometric crystal properties, as well as the detector radiopurity. Since this deviation from stoichiometry increases together with the contamination of the raw initial materials, their chemical purity impacts directly on the detector performance [6,7]. This is true in particular for bolometric detectors, where defects of the crystalline structure affect the phonon scattering in the crystal [11]. As a result the thermal conductivity of the detector decreases, causing a loss in energy resolution. It is therefore mandatory to use initial materials with superior chemical and radio-purity to obtain high-performance scintillating bolometers based on zinc-containing crystals.

In this work, we introduce a novel method for zinc purification (Sect. 2), validating the whole production through mass spectrometry (Sect. 3) and γ-spectroscopy (Sect. 4). The excellent radiopurity achieved allows us to search for double β-decay of ^{64}Zn, in particular neutrinoless and two-neutrino modes of electron capture with positron emission ($\varepsilon\beta^+$), as well as neutrinoless double electron capture ($0\nu 2\varepsilon$), setting the most stringent lower limits on their half-lives to date (Sect. 5).

2 A new process for zinc purification

The raw zinc, chosen with purity level higher than 99.98%, is prepared for the purification process trough the following steps: (i) cutting of initial metal ingot in order to get pieces of about 2 kg of mass, (ii) etching of Zn pieces in nitric acid solution (0.1 M HNO_3), (iii) washing of etched Zn pieces in ultra-pure water, (iv) drying of washed Zn pieces, and (v) sampling for tracing of contamination level by means of mass-spectrometry.

The actual purification process presented here consists then of two phases: (i) the refining of the initial zinc by filtration and distillation under vacuum, and (ii) the formation of granules of (3 - 5) mm in diameter by dripping of molten metal in the coolant agent. This last step modifies the material in a suitable form for the subsequent stages of crystal production.

The innovative method used to implement the first step has been developed at the National Science Center "Kharkov Institute of Physics and Technology" (Kharkov, Ukraine). The procedure involves the filtration of the molten metal and its subsequent distillation by condensing the metal steam into the solid phase [12]. The distillation process is carried out at a temperature $T_D = T_M + (40-50)\,^o$C, while the condensation process at a temperature $T_C = T_M - (30-40)\,^o$C, being $T_M = 419\,^o$C the melting temperature.

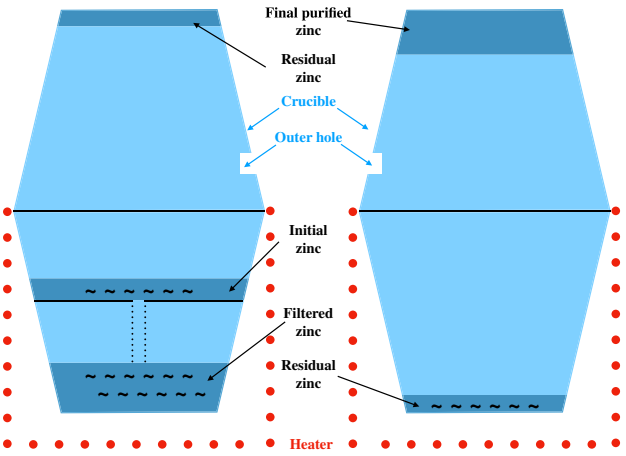

Fig. 1 Scheme of the set-up for zinc purification: **a** stage of filtration and refining against of the volatile impurities (left); **b** stage of purification against of the non-volatile impurities (right). We melt the initial zinc using a heater, obtaining the filtered zinc. We remove most of the volatile impurities through the outlet hole, while a small amount of them remains in the thin layer of condensed zinc, also removed. By further heating the sample, all zinc evaporates, forming a layer of purified zinc, while non-volatile impurities form a residue in the crucible

The distillation set-up is made from high-purity high-density graphite, characterized by chemical inertness to zinc and a minimal content of impurities. To further increase the graphite purity, the setup was thermally treated under vacuum at (1000–1100) ^{o}C before use. The concentration of all possible contaminants in the graphite was measured by spectral analysis, resulting in less than 1.0 ppm. The distillation set-up was assembled of two identical pieces, as shown in Fig. 1: the bottom one serves as a crucible, while the upper part is a collector for the condensed Zn metal. The small outlet hole in the lateral wall of the condenser is intended for evacuation in order to remove volatile impurities. The crucible is heated by the heater, while the condenser is heated indirectly by the thermal radiation of the crucible, as well as by the heat transfer from the stream of the distillable metal. The crucible volume was designed to hold 2.0 kg of loaded initial zinc. The operating pressure during zinc refining was about (10^{-3}–10^{-2}) Pa.

At the first stage, the purification process was carried out against volatile impurities (like a Na, K etc.) by their condensation on the inner surface of the condenser (see Fig. 1, left). A part of them is also removed continuously pumping the crucible volume through the outer hole. In order to remove oxides and other slags, the molten metal was filtered, through a plate with a small conicity and a hole in the middle. At the end of this stage, about 100 g of zinc metal containing a high concentration of the volatile impurities is removed from the coldest part of the condenser.

The second stage is carried out in order to remove the non-volatile impurities (like a Cu, Fe, Si, Ni, Co, V, Cr, Al,

Tl, Bi, Mn etc.) by distillation of the zinc metal, poured in the crucible after filtration. After evaporation (up to 95% of loaded material), the pure zinc is condensed on the inner part of the condenser, while the non-volatile impurities remain as residue on the bottom of the crucible (see Fig. 1, right). Such combination of refining stages significantly improves the efficiency of the whole purification process and product yield, which is better than 95% from the initial loaded zinc.

At the end of this process, the purified zinc was sent for the granulation in a dedicated device by dripping of the molten metal into high-purity water used as a cooling agent.[1] The final high-purity zinc was obtained in form of granules with 3–4 mm in diameter, achieving a 99% yield for the granulation process. We obtained 15 kg of ultra-pure zinc after eight purification cycles (2 kg of Zn each), with a final yield of 94%.

3 Results of refinement

We did a general comparative analysis of elemental impurities in the zinc metal before and after purification by combining the Laser (LMS) and Inductively Coupled Plasma (ICP) Mass-Spectrometry methods. While the chemical purity of the initial zinc metal was studied at NSC KIPT (Kharkov, Ukraine) using a High-Resolution Double-Focusing Laser Mass-Spectrometer EMAL-2 by Mattauch-Herzog, the residual contamination of the purified metal was examined with the help of High-Resolution Inductively Coupled Plasma-Mass Spectrometric analysis (HR-ICP-MS, Thermo Fisher Scientific ELEMENT2) at the Gran Sasso Laboratory (Assergi, Italy). To reduce cosmogenic activation, we have shipped the zinc from Ukraine to Italy by land.

As can be seen from the comparison reported in Table 1, the developed purification method is very effective for the entire range of impurity elements. For most elements the concentration was reduced by one to two orders of magnitude. For example, the iron concentration was reduced by about 500 times, whereas potassium was reduced by a factor of 85. Not listed elements have concentrations which are limited by the instrumental detection level. Cadmium is the contaminant limiting the purity of material its concentration was reduced only about 5 times with a final concentration of 4 ppm. This can be explained by two reasons. First, zinc and cadmium are similar from the chemical point of view. Second, at the distillation temperature of zinc, about (460 - 470) ^{o}C, cadmium and zinc have very similar vapor pressures. As a consequence, cadmium transits almost completely into the condensate of zinc. The mass fraction of the final purified zinc was determined as the difference between 100% and the total content of major impurities (Cd, Fe, Si, Al, Na, K and Ca). The obtained value is higher than 99.999%, which meets the requirement on the chemical purity of the materials used for the production of high-quality crystals.

Table 1 Impurity concentration in the zinc before and after the purification process in ppb (10^{-9} g/g) with uncertainties of 25%

Element	Initial zinc	Purified zinc
Na	1000	30
Al	4000	35
Si	7000	40
K	3000	35
Ca	2000	70
V	< 200	< 9
Cr	< 200	< 90
Mn	< 200	< 90
Fe	30,000	56
Co	< 200	< 10
Ni	< 300	< 90
Cu	10,000	110
Mo	< 2000	4
Cd	20,000	4300
Sn	15,000	< 300
Tl	< 2000	180
Pb	< 3000	290
Bi	< 1000	< 2
Th	< 2000	< 0.2
U	< 2000	< 0.2

4 Low background measurement with HPGe detector

In order to measure the internal radioactive contaminations of the purified granular zinc, we perform a γ-spectrometry measurement with an ultra-low background high purity germanium detector (ULB-HPGe). We carried out this activity in the STELLA (SubTerranean Low-Level Assay) facility at Gran Sasso National Laboratories (Italy), characterized by an average shielding of 3600 m.w.e., details can be found in Refs. [13–16].

The ULB-HPGe detector is a coaxial p-type germanium detector with an active volume of about 400 cm^3 and an optimized design for high counting efficiency in a wide energy range. The energy resolution of the spectrometer is 2.0 keV at the 1332 keV line of ^{60}Co. To reduce external background, the detector is shielded with a 20 cm layer of low-radioactivity lead, OFHC (Oxygen Free High Conductivity) copper ($\sim$5 cm) and a 5 cm layer of Polyethylene. To prevent radon contamination, the set-up is continuously flushed with

[1] Patent on metal granulation N. 131214 Ukraine – Publ. 01/10/2019 – Bull. N. 1 - By A.P Shcherban, Yu.V. Gorbenko, G.P. Kovtun, D.A. Solopikhin.

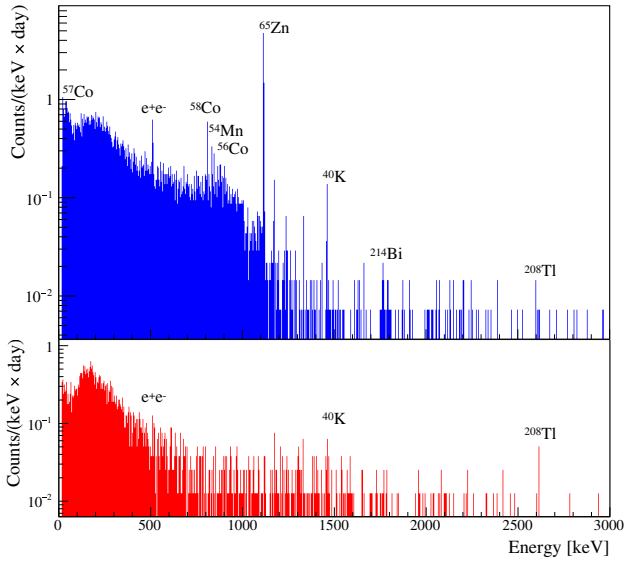

Fig. 2 Energy spectrum acquired with the GeMPI-4 ULB-HPGe spectrometer with 10.08 kg of natural zinc over 827.66 h (top), and without the Zn sample over 474.35 h (bottom)

Table 2 Activity of internal radioactive contaminations in the purified granular zinc measured with a ULB-HPGe detector. Activity values are present in units of mBq/kg, and limits are at 90% CL

Chain	Nuclide	Activity (mBq/kg)
^{232}Th	^{228}Ra	< 0.095
	^{228}Th	< 0.036
^{238}U	^{234}Th	< 6.2
	^{234m}Pa	< 4.7
	^{226}Ra	< 0.066
^{235}U	^{235}U	< 0.091
	^{40}K	<0.38
	^{60}Co	< 0.036
	^{137}Cs	< 0.033
	^{54}Mn	0.11 ± 0.02
	^{56}Co	0.08 ± 0.02
	^{57}Co	0.20 ± 0.09
	^{58}Co	0.22 ± 0.04
	^{65}Zn	5.2 ± 0.6

high-purity boil-off nitrogen. More details on the experimental set-up and detector performance can be found in Ref. [17].

We placed a sample of the purified granular zinc with a mass of 10,080 g in a polypropylene container of Marinelli geometry (GA-MA Associates, type 441G) above the endcap of the ULB-HPGe detector. We measured the Zn sample for 827.66 h, whilst background data was accumulated over 474.35 h. Figure 2 shows the energy spectra of the two measurements.

The efficiencies for the full-energy absorption peaks used for the quantitative analysis are obtained by Monte-Carlo simulation (code MaGe), based on the GEANT4 software package [18].

We report in Table 2 the list of internal radioactive nuclides found in the sample. These values are obtained using the procedure presented in Ref. [19]. We found no evidence of any daughter nuclides from the natural decay chains of ^{235}U, ^{238}U and ^{232}Th, so that we set upper limits on the level of less than few mBq/kg. We also report the limits on the activity of other commonly observed nuclides, in particular for ^{40}K, from natural radioactivity, ^{60}Co, produced by cosmogenic activation, and artificial ^{137}Cs. However, we measure significant activity of some specific isotopes such as ^{54}Mn, ^{56}Co, ^{57}Co, ^{58}Co and ^{65}Zn at mBq/kg level. Those isotopes are produced by cosmogenic activation via neutron spallation on naturally occurring zinc isotopes. Among the listed isotopes, ^{54}Mn is the most long-lived nuclide that decays via electron capture with a Q-value (Q_{EC}) of 1377.1 keV and a half-life of 312.12 d. However, the relatively small released energy in this decay makes it not dangerous for exploring of 2β decay of the most common isotopes. The same holds for ^{57}Co ($T_{1/2}$ = 271.79 d, Q_{EC} = 836 keV), ^{58}Co ($T_{1/2}$ = 70.85 d, Q_{EC} = 2307.4 keV) and ^{65}Zn ($T_{1/2}$ = 244.26 d, Q_{EC} = 1351.9 keV). ^{56}Co decays through electron capture with a Q-value of 4566.0 keV, but the relatively short half-life (77.27 d) makes it disappear quickly.

These results are confirmed by the CUPID-0 experiment since its ZnSe crystals were made from the zinc measured in this work and the selenium 95% enriched in ^{82}Se [20]. Indeed the CUPID-0 background model [21] attributes to ZnSe crystal contaminations much smaller values than the limits reported in this analysis, suggesting that probably during the crystals growth the contaminant segregation further help the purification process. The excellent radiopurity level reached by implementing this technique allowed CUPID-0 to get the lowest background index among cryogenic calorimeters of 3.5×10^{-3} counts/(keV·kg·year) [22], and several scientific results [22–26].

5 Double beta processes in Zn-64

Natural zinc contains two potentially 2β-decaying isotopes, ^{64}Zn and ^{70}Zn, whose features are reported in Table 3. The ^{70}Zn decay would not involve excited states of ^{70}Ge [27] and only two electrons sharing the $Q_{\beta\beta}$ energy would be emitted, preventing the decay detection with a HPGe detector. On the contrary, characteristic γ-rays can be emitted in $\varepsilon\beta^+$ and 2ε decays of ^{64}Zn, thus providing distinctive signatures suitable for HPGe spectroscopy.

The CUPID-0 experiment has recently set a new limit $0\nu\varepsilon\beta^+$ of ^{64}Zn [28], taking advantage of the ability, offered

Table 3 Potentially double beta decaying isotopes of zinc and their features

Isotope	Isotopic abundance (%)	Decay mode	Q-value (keV)
^{64}Zn	47.55 (0.18)	$\varepsilon\beta^+/2\varepsilon$	1094.9 (0.8)
^{70}Zn	0.68 (0.02)	$2\beta^-$	997.1 (2.1)

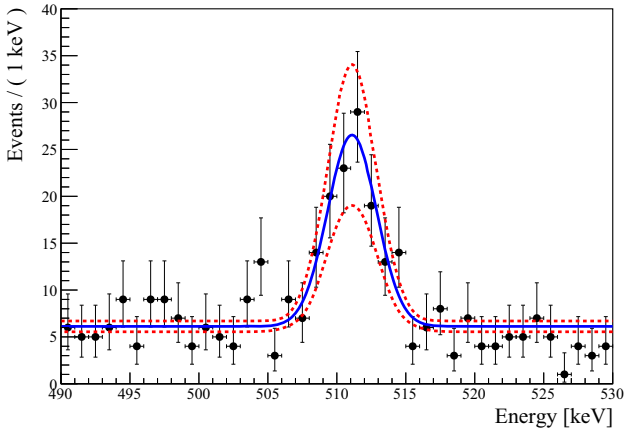

Fig. 3 Energy spectra focused on 511 keV peak. Data acquired by the GeMPI-4 ULB-HPGe spectrometer with the zinc sample over 827.66 h. The blue line marks the best fit result, while the red dashed lines report a 1 σ statistical fluctuation of the number of counts of all the contributions

by the calorimetric approach, to measure the whole $Q_{\varepsilon\beta^+}$ energy. We report in this section a complementary analysis which investigates the decay modes not covered by CUPID-0.

5.1 $\varepsilon\beta^+$ decay mode

^{64}Zn can decay via electron capture with positron emission:

$$^{64}\mathrm{Zn} + e^- \longrightarrow {}^{64}\mathrm{Ni} + E_{\text{de-exitation}} + e^+ \ (+2\,\nu_e) \tag{1}$$

where $E_{\text{de-exitation}}$ is carried by the X-rays or Auger electrons emitted after the capture. In both 0ν and 2ν cases, the emitted positron generates two 511 keV γs, leading to an extra counting rate in the annihilation peak on the total energy spectrum. Since it is impossible to distinguish the two decay modes, we can set a limit for the combination of these two processes. Exploiting a Monte-Carlo simulation, we evaluate the detection efficiency in the experimental setup of a 511 keV γ-ray, obtaining $\eta_{\varepsilon\beta^+} = 1.3\%$. Despite the low efficiency, the high ^{64}Zn isotopic abundance equal to $(47.55 \pm 0.18)\%$ guarantees a large number of emitting isotopes in the sample ($N_{^{64}\mathrm{Zn}} = 4.41 \times 10^{25}$ nuclei), achieving a total exposure of $N_{\text{exp}} = (4.17 \pm 0.02) \times 10^{24}$ emitters$\times$year.

The analysis strategy consists of a Binned Extended Likelihood fit that takes into account all the background sources contributing to the 511 keV peak, selecting as region of interest the energy range [490,530] keV (Fig. 3). The model function $\mathcal{F}_{\varepsilon\beta^+}$ is composed of a Gaussian peak over a flat background,

$$\mathcal{F}_{\varepsilon\beta^+} = N_{511} \cdot \mathcal{G}(\mu, \sigma) + N_{\text{b}} \tag{2}$$

where

$$N_{511} = N_{511}^{\text{sig}} + N_{511}^{^{65}\mathrm{Zn}} + N_{511}^{^{58}\mathrm{Co}} + N_{511}^{^{56}\mathrm{Co}} \tag{3}$$

$$N_{511}^{\text{sig}} = \Gamma_{\varepsilon\beta^+} \cdot \eta_{\varepsilon\beta^+} \cdot N_{\text{exp}} \tag{4}$$

The total number of counts of the peak (N_{511}) is given by the sum of the expected background events, previously evaluated with a MC simulation assuming the activities in Table 2, and the possible signal one. The largest contribution into the annihilation peak comes from the decay of ^{65}Zn with $N_{511}^{^{65}\mathrm{Zn}} = (60 \pm 6)$ counts, while ^{58}Co and ^{56}Co produce $N_{511}^{^{58}\mathrm{Co}} = (22 \pm 4)$ and $N_{511}^{^{56}\mathrm{Co}} = (13 \pm 4)$ counts, respectively. For all these contributions, we assume a Gaussian prior with the mean and width set to the best estimated values and uncertainties, respectively. The events induced by other isotopes listed in Table 2 are effectively included in the flat background (N_{b}). As a consistency check, we modelled the background with an exponential function, whose coefficient resulted to be statistically compatible with zero. Thus we decided to reduce the number of free parameters exploiting a flat background, which gave a more conservative limit.

The best fit result is $\Gamma_{\varepsilon\beta^+} = (-0.06 \pm 1.37) \times 10^{-22}$ year^{-1} compatible with zero, thus no significant excess of events was found. We perform a Bayesian analysis integrating the likelihood with a uniform prior and marginalising over the nuisance parameters to set a limit on the half-life of $(0\nu + 2\nu)\varepsilon\beta^+$. This is done exploiting the RooStat Bayesian Calculator tools. The resulting upper limit on the decay rate at 90% CI is $\Gamma_{\varepsilon\beta^+} < 2.56 \times 10^{-22}$ year^{-1}, corresponding to a lower-limit on the half-life,

$$T_{1/2}^{\varepsilon\beta^+} > 2.7 \times 10^{21} \text{ year} \quad \text{at } 90\% \text{ CI} \tag{5}$$

This result is almost a factor three better than the previous limit on the half-life of $2\nu\varepsilon\beta^+$, equal to $T_{1/2} > 9.4 \times 10^{20}$ year at 90% CL [29]. For the $0\nu\varepsilon\beta^+$ a more stringent limit was set by CUPID-0 equal to 1.2×10^{22} year at 90% CI [28].

5.2 2ε decay mode

The ^{64}Zn can decay via double electron capture into the ground state of ^{64}Ni with the same Q-value as of the $\varepsilon\beta^+$ mode, (1094.9 ± 0.8) keV:

$$^{64}\mathrm{Zn} + 2\,e^- \longrightarrow {}^{64}\mathrm{Ni} + \gamma_{\text{de-exitation}} \ (+2\,\nu_e) \tag{6}$$

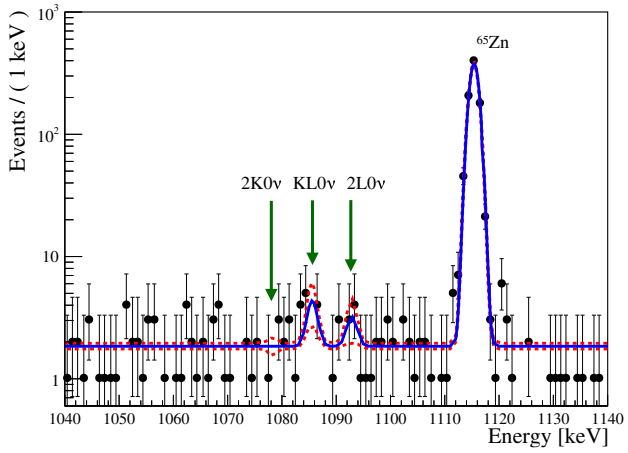

Fig. 4 Energy spectrum focused on $0\nu2\varepsilon$ ROI. The peak at 1115 keV is given by the ^{65}Zn decay. The blue line marks the best fit result, while the red dashed lines report a 1σ statistical fluctuation of the number of counts of all the contributions

The $2\nu2\varepsilon$ capture is not considered here because in this case only low energy X-rays are emitted (E = 0.9–8.3 keV), which are effectively absorbed by the Zn sample itself. On the other hand, when a $0\nu2\varepsilon$ occurs, we can assume X-rays are accompanied by a bremsstrahlung γ-quantum with $E_\gamma = Q - E_{b1} - E_{b2}$ [30–32], where E_{b1} and E_{b2} are the binding energy of two captured electrons on the corresponding atomic shells of ^{64}Ni. For Ni atoms, the binding energies on the K and L1 shells are equal to $E_K = 8.3$ keV and $E_{L1} = 1.01$ keV, respectively.

Thus, the expected energy of the γs for the $0\nu2\varepsilon$ capture ^{64}Zn to ground state of ^{64}Ni is equal to: (i) $E_1 = 1079.0$ keV for $2K0\nu$; (ii) $E_2 = 1086.4$ keV for $KL0\nu$; and (iii) $E_3 = 1093.7$ keV for $2L0\nu$ processes.

As in the previous case, a Monte Carlo simulation provides the detection efficiency for gammas of these energies, corresponding to $\eta_{2\varepsilon} = 1.1\%$, while the exposure remains the same with respect to the previous analysis. Since the atomic mass difference ^{64}Zn^{64}Ni is currently known with an uncertainty of 0.8 keV, the positions of the expected $0\nu2\varepsilon$ peaks will have the same uncertainty. Figure 4 shows the energy spectrum acquired with the zinc sample in the range [1040,1140] keV. Also in this case, we perform a Binned Extended Likelihood fit on the data. The model function $\mathcal{F}_{0\nu2\varepsilon}$ is composed of a flat background and four Gaussian distributions, three of which represent the expected signal and are centered in $\mu_i = E_i$ $(i = 1, 2, 3)$, while the fourth reproduces the ^{65}Zn peak at 1115 keV,

$$\mathcal{F}_{0\nu2\varepsilon} = \sum_{i=1}^{3} N_i \cdot \mathcal{G}(\mu_i, \sigma) + N_{^{65}\mathrm{Zn}} \cdot \mathcal{G}(\mu, \sigma) + N_\mathrm{b} \qquad (7)$$

where

$$N_i = \Gamma^i_{0\nu2\varepsilon} \cdot \eta_{2\varepsilon} \cdot N_\mathrm{exp} \qquad (8)$$

$$\Gamma_{0\nu2\varepsilon} = \sum_{i=1}^{3} \Gamma^i_{0\nu2\varepsilon} \qquad (9)$$

We fix the means of the three signal peaks and successively include their uncertainty in the nuisance parameters with a normal prior. We assume all the peaks have the same energy resolution, which is accurately determined on the ^{65}Zn peak. Since the relative probability of double electron capture from the K and L shells is not available in literature [33], we do not apply any constrain on N_i, considering the three signatures as independent contributions to the decay rate $\Gamma_{0\nu2\varepsilon}$.

We observe an excess of events at the $KL0\nu$ peak, but the statistical significance ($1.6\ \sigma$) is not such as to suggest the observation of the decay. Following the same procedure as the previous analysis, we set a limit on the decay rate of $\Gamma_{0\nu2\varepsilon} < 2.69 \times 10^{-22}$ year^{-1} at 90% CI, corresponding to a limit on the half-life of

$$T^{0\nu2\varepsilon}_{1/2} > 2.6 \times 10^{21} \text{ year} \quad \text{at } 90\% \text{ CI} \qquad (10)$$

This result surpasses by almost one order of magnitude the previous limit, $T^{0\nu2\varepsilon}_{1/2} > 3.2 \times 10^{20}$ year at 90% CL [29].

6 Conclusions

In this work, we established an innovative technique for high-purity zinc production, based on the combination of filtration and distillation to remove volatile and non-volatile contaminants.

We produced 15 kg of granular zinc with purity grade more than 99.999%, which was delivered by land transportation to LNGS, where it was characterized with ICP-MS and HPGe spectroscopy. The achieved chemical purity, with a total concentration of entire contaminants less than 10 ppm, completely meets the requirements for the growth of high-quality large-volume crystals. The presence of naturally occurring radio nuclides is excluded, with measured upper limits of few mBq/kg. The only significant radioactive contamination is on the level of few mBq/kg and is due to cosmogenic isotopes.

The excellent radiopurity of the zinc sample allowed us to set the most stringent limits to date on the ^{64}Zn $2\nu\varepsilon\beta^+$ and $0\nu2\varepsilon$ decay modes, resulting in $T^{\varepsilon\beta^+}_{1/2} > 2.7 \times 10^{21}$ year , and $T^{0\nu2\varepsilon}_{1/2} > 2.6 \times 10^{21}$ year , respectively. Exploiting the advantages of spectroscopy with an external source, we overcome the technical difficulty of the CUPID-0 experiment in studying these decays [28] by carrying out a complementary measurement. The limits obtained both in this work and from

CUPID-0 are still several orders of magnitude lower than theoretical predictions [34,35], so new experimental efforts are needed to investigate these processes.

Acknowledgements This work was partially supported by the European Research Council (FP7/2007-2013) under contract LUCIFER No. 247115.

Data Availability Statement This manuscript has no associated data or the data will not be deposited. [Authors' comment: The data will be available at any time by contacting the Corresponding Author.]

Funded by SCOAP[3].

References

1. M. Tanabashi et al., Phys. Rev. D **98**, 030001 (2018). https://doi.org/10.1103/PhysRevD.98.030001
2. M.J. Dolinski, A.W. Poon, W. Rodejohann, Annu. Rev. Nucl. Part. Sci. **69**, 219 (2019). https://doi.org/10.1146/annurev-nucl-101918-023407
3. A. Barabash et al., J. Instrum. **15**(07), C07037 (2020). https://doi.org/10.1088/1748-0221/15/07/c07037
4. A. Barabash et al., Nucl. Instrum. Meth. Phys. Res. Section A: Accel. Spectrom. Detect. Assoc. Equip. **833**, 77 (2016). https://doi.org/10.1016/j.nima.2016.07.025
5. P. Belli et al., Nucl. Instrum. Meth. Phys. Res. Section A: Accel. Spectrom. Detect. Assoc. Equip. **935**, 89 (2019). https://doi.org/10.1016/j.nima.2019.05.014
6. O. Azzolini et al., Eur. Phys. J. C **78**(5), 428 (2018). https://doi.org/10.1140/epjc/s10052-018-5896-8
7. E. Armengaud et al., Eur. Phys. J. C **77**(11), 785 (2017). https://doi.org/10.1140/epjc/s10052-017-5343-2
8. J. Ebert et al., Phys. Rev. C **94**(2), 024603 (2016). https://doi.org/10.1103/PhysRevC.94.024603
9. I. Dafinei et al., J. Cryst. Growth **475**, 158 (2017). https://doi.org/10.1016/j.jcrysgro.2017.06.013
10. M. Manutchehr-Danai (ed.), *Bridgman–Stockbarger Technique* (Springer, Berlin, 2009), pp. 111–111. https://doi.org/10.1007/978-3-540-72816-0_2926
11. E.A. Scott, K. Hattar, C.M. Rost, J.T. Gaskins, M. Fazli, C. Ganski, C. Li, T. Bai, Y. Wang, K. Esfarjani, M. Goorsky, P.E. Hopkins, Phys. Rev. Mater. **2**, 095001 (2018). https://doi.org/10.1103/PhysRevMaterials.2.095001
12. G. Kovtun, A. Shcherban, D. Solopikhin, V. Virich, V. Zelenskaya, R. Boiko, F. Danevich, V. Mokina, S. Nagorny, Funct. Mater. **18**, 121 (2011)
13. C. Arpesella, Appl. Radiat. Isot. **47**(9), 991 (1996). https://doi.org/10.1016/S0969-8043(96)00097-8. Proceedings of the International Committee for Radionuclide Metrology Conference on Low-level Measurement Techniques
14. H. Neder, G. Heusser, M. Laubenstein, Appl. Radiat. Isot. **53**(1), 191 (2000). https://doi.org/10.1016/S0969-8043(00)00132-9
15. G. Heusser, M. Laubenstein, H. Neder, in *Radionuclides in the Environment*, *Radioactivity in the Environment*, vol. 8, ed. by P. Povinec, J. Sanchez-Cabeza (Elsevier, 2006), pp. 495 – 510. https://doi.org/10.1016/S1569-4860(05)08039-3
16. D. Budjáš, W. Hampel, M. Heisel, G. Heusser, M. Keillor, M. Laubenstein, W. Maneschg, G. Rugel, S. Schönert, H. Simgen, H. Strecker, Highly sensitive gamma-spectrometers of gerda for material screening: Part **2** (2008)
17. M. Laubenstein, Int. J. Mod. Phys. A **32**(30), 1743002 (2017). https://doi.org/10.1142/S0217751X17430023
18. M. Boswell et al., IEEE Trans. Nucl. Sci. **58**(3), 1212 (2011). https://doi.org/10.1109/TNS.2011.2144619
19. M. Heisel, F. Kaether, H. Simgen, Appl. Radiat. Isot. **67**(5), 741 (2009). https://doi.org/10.1016/j.apradiso.2009.01.028. 5th International Conference on Radionuclide Metrology - Low-Level Radioactivity Measurement Techniques ICRM-LLRMT'08
20. J. Beeman et al., Eur. Phys. J. C **75**(12), 591 (2015). https://doi.org/10.1140/epjc/s10052-015-3822-x
21. O. Azzolini et al., Eur. Phys. J. C **79**(7), 583 (2019). https://doi.org/10.1140/epjc/s10052-019-7078-8
22. O. Azzolini et al., Phys. Rev. Lett. **123**(3), 032501 (2019). https://doi.org/10.1103/PhysRevLett.123.032501
23. O. Azzolini et al., Phys. Rev. Lett. **120**(23), 232502 (2018). https://doi.org/10.1103/PhysRevLett.120.232502
24. O. Azzolini et al., Eur. Phys. J. C **78**(11), 888 (2018). https://doi.org/10.1140/epjc/s10052-018-6340-9
25. O. Azzolini et al., Phys. Rev. Lett. **123**(26), 262501 (2019). https://doi.org/10.1103/PhysRevLett.123.262501
26. O. Azzolini et al., Phys. Rev. D **100**(9), 092002 (2019). https://doi.org/10.1103/PhysRevD.100.092002
27. J. Leske, K.H. Speidel, S. Schielke, J. Gerber, P. Maier-Komor, S.J.Q. Robinson, A. Escuderos, Y.Y. Sharon, L. Zamick, Phys. Rev. C **74**, 024315 (2006). https://doi.org/10.1103/PhysRevC.74.024315
28. O. Azzolini et al., Eur. Phys. J. C **80**(8), 702 (2020). https://doi.org/10.1140/epjc/s10052-020-8280-4
29. P. Belli et al., J. Phys. G Nucl. Part. Phys. **38**(11), 115107 (2011). https://doi.org/10.1088/0954-3899/38/11/115107
30. R.G. Winter, Phys. Rev. **100**, 142 (1955). https://doi.org/10.1103/PhysRev.100.142
31. F. Danevich, M. Hult, D. Kasperovych, G. Kovtun, K. Kovtun, G. Lutter, G. Marissens, O. Polischuk, S. Stetsenko, V. Tretyak, Nucl. Phys. A **996**, 121703 (2020). https://doi.org/10.1016/j.nuclphysa.2020.121703
32. A. Barabash, V. Brudanin, A. Klimenko, S. Konovalov, A. Rakhimov, E. Rukhadze, N. Rukhadze, Y. Shitov, I. Stekl, G. Warot, V. Umatov, Nucl. Phys. A **996**, 121697 (2020). https://doi.org/10.1016/j.nuclphysa.2020.121697
33. K. Blaum, S. Eliseev, F.A. Danevich, V.I. Tretyak, S. Kovalenko, M.I. Krivoruchenko, YuN Novikov, J. Suhonen, Neutrinoless double-electron capture. Rev. Mod. Phys. **92**, 045007 (2020). https://doi.org/10.1103/RevModPhys.92.045007
34. P. Domin, S. Kovalenko, F. Simkovic, S. Semenov, Nucl. Phys. A **753**, 337 (2005). https://doi.org/10.1016/j.nuclphysa.2005.03.003
35. E.W. Grewe et al., Phys. Rev. C **77**, 064303 (2008). https://doi.org/10.1103/PhysRevC.77.064303